Separation Control Using Moving Surface Effects: A Numerical Simulation

A. A. Hassan*
McDonnell Douglas Helicopter Company, Mesa, Arizona 85205
and
L. N. Sankar†
Georgia Institute of Technology, Atlanta, Georgia 30332

A numerical study is conducted to investigate the effects of forebody boundary-induced vorticity (FBIV) on the development of the laminar/turbulent boundary layers over modified NACA 0012, NACA 63-218 airfoils having leading-edge rotation. Here, we utilize an implicit finite-difference procedure to solve the two-dimensional compressible full Reynolds-averaged Navier-Stokes equations on a body-fitted curvilinear coordinate system. For the subcritical and supercritical flows considered, convergence to steady state is expedited through the use of locally varying time steps. Of special interest to the present study is the effect of varying the leading-edge circumferential speed, and, hence, the strength of the FBIV, on the following: 1) location of the point(s) of laminar and/or turbulent separation, 2) the size of the separated flow region above the airfoil, 3) the strength and location of shock waves, and 4) the computed sectional lift coefficients. Similar to circulation control airfoils, for subcritical onset flows, numerical results have indicated that with such a leading-edge device, aerodynamic lift forces can be augmented without the need to change the airfoil's angle of attack and/or chord Reynolds number. Qualitative comparisons with smoke wire flow visualization results and available experimental data are presented.

Nomenclature

A = Jacobian matrix of the flux vector E
a = normalized local speed of sound
B = Jacobian matrix of the flux vector F
c = airfoil chord length
E = flux vector in the x direction
e = total energy per unit volume
F = flux vector in the y direction
I = identity matrix
i = grid node index along the ξ direction
J = Jacobian of the numerical transformation
j = grid node index along the η direction
M = local Mach number
n = index for time step
p = normalized local pressure
q = vector representing the dependent variables
R,S = vectors containing viscous terms
t or τ = nondimensional time
U,V = contravariant velocities
u,v = normalized Cartesian velocities
W = circumferential velocity of rotating leading edge
x,y = Cartesian physical plane coordinates
β = Mach number associated with rotating leading edge
γ = ratio of specific heats
Δ, ∇ = forward and backward differencing operators, respectively
δ = central difference operator
θ = local slope of airfoil surface
ξ, η = computational plane coordinates
ρ = normalized local density

Presented as Paper 89-0972 at the AIAA 2nd Shear Flow Conference, Tempe, AZ, March 13-16, 1989; received Sept. 16, 1989; revision received Nov. 30, 1990; accepted for publication Dec. 7, 1990. Copyright © 1991 by the American Institute of Aeronautics and Astronautics, Inc. All rights reserved.

*Manager, Aerodynamics/Acoustics. Member AIAA.
†Associate Professor, School of Aerospace Engineering. Member AIAA.

Introduction

BOUNDARY-LAYER control (BLC) technology has undergone tremendous progress in recent years due to the focused research efforts in the areas of aerodynamics, structures, and materials. This major experimental effort has been made in aerodynamics not only because it has been experimentally convenient, but more importantly because of the very strong influence boundary-layer separation and transition have on many aerodynamic characteristics. For example, attached laminar flow over major portions of an aircraft wing has long been known to have favorable effects in terms of aerodynamic performance and fuel economy. On the other hand, it has been observed experimentally[1-3] that, at high angles of attack (e.g., during takeoff or while performing a sharp maneuver), the flow tends to separate from the upper surface of the wing, resulting in a significant reduction in the attainable lift and a considerable increase in the overall drag of the aircraft. Since the maximum usable lift is an important ingredient in high angle-of-attack maneuvering for combat aircraft and in determining the maximum payloads for commercial and rotary wing aircraft, BLC techniques and lift augmentation devices have been a focus of extensive experimental research over the past 30 years.

To alleviate the problems arising from the separation of the boundary layer, control methods disrupting the natural mechanism(s) leading to separation (e.g., suction[4] and blowing[5]) have been investigated at length and employed in practice with a varying degree of success. Nevertheless, irrespective of the BLC method used, the ultimate goal is to delay or perhaps prevent the separation of the boundary layer from the solid surface. A vast body of literature pertaining to boundary-layer control has been reviewed by several authors, including Lachmann,[6] Rosenhead,[7] Schlichting,[8] and Chang.[9]

In this paper, we numerically investigate an alternate approach, referred to in the literature as the "moving-wall," to control or disrupt the natural mechanism(s) leading to the

separation of the laminar and/or turbulent boundary layers over an airfoil. In this respect, the aerodynamic forces are augmented as a consequence of the wall-jet-like effect resulting from the motion of a segment of the solid boundary. Kothari and Anderson[10] have shown that, if an airfoil is placed in a uniform stream at an angle of attack approaching the static stall angle, then the suction side flowfield will be primarily dominated by a highly organized vortical-type flow. Under such conditions, the vorticity shed from the airfoil's leading edge manifests itself in a number of primary vortices situated above the airfoil. To disrupt the formation of such vortices, it is obvious that vorticity with opposite sign to that being shed must be introduced at the leading edge. In this study, the introduced vorticity is being generated through the motion of a small segment of the solid boundary of the airfoil (accomplished here by a rotating cylindrical leading edge). The direction of rotation is from the pressure side of the airfoil to its suction side. The resulting flowfield is, therefore, a complex one resulting from the strong interaction, in the presence of a pressure gradient, between the naturally generated leading-edge vortical flow and the additional vortical flow resulting from the motion of the solid surface.

In consideration of the effects of the moving surface on boundary-layer separation, experiments carried out by a number of investigators[11-13] concentrated on studying the effects of the rotating leading edge on the measured aerodynamic force and moment coefficients. These experiments, although quantitative in nature, provide information about the character and behavior of the boundary layer only in a "general" sense. The numerical simulations conducted by Moktarian and Modi,[14] using the surface singularity approach with viscous corrections, is promising. However, the approach is limited to flows that do not contain regions of massive boundary-layer separation and, therefore, is not suitable for the analysis of flows at angles of attack approaching or exceeding the static stall angle.

To partially address this absence, numerical simulations of the laminar and/or turbulent flows past modified NACA 0012 and NACA 63-218 airfoils having leading-edge rotation have been performed (using a modified version of the McDonnell Douglas Helicopter Company two-dimensional Navier-Stokes solver DSS2) for a wide range of angles of attack, leading-edge rotation speeds, and freestream Mach numbers. Here, an approximate factorization (AF) finite-difference solution procedure is used to numerically integrate the unsteady, two-dimensional, compressible full Reynolds-averaged Navier-Stokes equations on a body conforming C-type grid. The Baldwin-Lomax[15] two-layer algebraic eddy viscosity model was incorporated in the present formulation to model turbulent shear stresses. In our simulations, transition to turbulence was assumed to occur at the airfoil's leading edge. This assumption, as will be seen later, is based on our experimental observations for the flow past the modified NACA 0015 airfoil. The present paper addresses the effects of varying the leading-edge circumferential speed, or, equivalently, the strength of the introduced forebody vorticity, on the following: location(s) of the points of laminar and/or turbulent separation on the airfoil's surfaces, the size of the separated flow regions, strength of shock waves for supercritical freestream Mach numbers, and the predicted sectional lift forces. For contrast, the results for the airfoil with leading-edge rotation are compared to those for the same airfoil without leading-edge rotation. Quantitative and qualitative comparisons with experimental results and smoke wire flow visualization results are also presented.

Mathematical Formulation

We consider two-dimensional unsteady compressible flow of a perfect gas. The flowfield is determined by the solution of the full Reynolds-averaged Navier-Stokes equations. In nondimensional conservation vector form, they may be written as

$$\partial_t q + \partial_x E + \partial_y F = Re^{-1}(\partial_x R + \partial_y S) \tag{1}$$

where

$$q = \begin{bmatrix} \rho \\ \rho u \\ \rho v \\ e \end{bmatrix}, \quad E = \begin{bmatrix} \rho u \\ \rho u^2 + p \\ \rho vu \\ u(e+p) \end{bmatrix}, \quad F = \begin{bmatrix} \rho v \\ \rho uv \\ \rho v^2 + p \\ v(e+p) \end{bmatrix}$$

$$R = \begin{bmatrix} 0 \\ \tau_{xx} \\ \tau_{xy} \\ R_4 \end{bmatrix}, \quad S = \begin{bmatrix} 0 \\ \tau_{xy} \\ \tau_{yy} \\ S_4 \end{bmatrix} \tag{2}$$

and

$$\tau_{xx} = \mu(\lambda + 2\mu)u_x + \lambda v_y \tag{3a}$$

$$\tau_{xy} = \mu(u_y + v_x) \tag{3b}$$

$$\tau_{yy} = (\lambda + 2\mu)v_y + \lambda u_x \tag{3c}$$

$$R_4 = u\tau_{xx} + v\tau_{xy} + \mu Pr^{-1}(\gamma - 1)^{-1}\partial_x a^2 \tag{3d}$$

$$S_4 = u\tau_{xy} + v\tau_{yy} + \mu Pr^{-1}(\gamma - 1)^{-1}\partial_y a^2 \tag{3e}$$

In Eqs. (2), the density ρ and velocity components u, v are normalized by the freestream density and speed of sound, respectively; the length scales x, y by the airfoil chord length c; time t by the ratio of the freestream speed of sound to the chord; and the total energy per unit volume e by the dynamic pressure based on the freestream speed of sound. In Eq. (1), Re is the Reynolds number (based on the airfoil's chord length, the freestream speed of sound and density), and, in Eqs. (3), Pr is the Prandtl number. Under Stokes hypothesis, the bulk viscosity λ is taken as $-(2/3)\mu$. For a calorically perfect gas, the equation of state may be written in nondimensional form as

$$p = (\gamma - 1)[e - 0.5\rho(u^2 + v^2)] \tag{4}$$

Moreover, the local speed of sound a is given by

$$a^2 = \gamma p \rho^{-1}$$

or, after utilizing Eq. (4), as

$$a^2 = \gamma(\gamma - 1)[e/\rho - 0.5(u^2 + v^2)] \tag{5}$$

To properly represent the physical domain of interest, and to facilitate the application of the physical slip and no-slip boundary conditions on the different segments of the airfoil's surface, it is important that the airfoil's surface coincide with one of the coordinate family of lines. In this respect, a body-fitted nonorthogonal coordinate system, referred to here as the ξ-η coordinate system, was utilized in the present formulation of the problem. The body-fitted grid was generated using an algebraic procedure[17] that results in a sheared parabolic C-type grid (see Figs. 1 and 2). To resolve the details of the flow in the developing boundary layer, an exponential stretching was used in the η direction, yielding a minimum normal grid spacing of $0.00005c$ between the surface grid points and the grid points in the flowfield just off the surface of the airfoil. This normal spacing, equivalent to a nondimensional law-of-the-wall coordinate $y^+ = 4$, has been shown to yield accurate results[15,16] when used in conjunction with the Baldwin-Lomax turbulence model.

The results reported here were obtained on a grid having 157 nodes in the wrap-around direction with 97 nodes on the surface of the airfoil, and 58 nodes in the normal direction with approximately 25 points submerged in the developing boundary layer. The outer far-field boundary was located at a distance approximately $8.5c$ away from the surface. With ξ

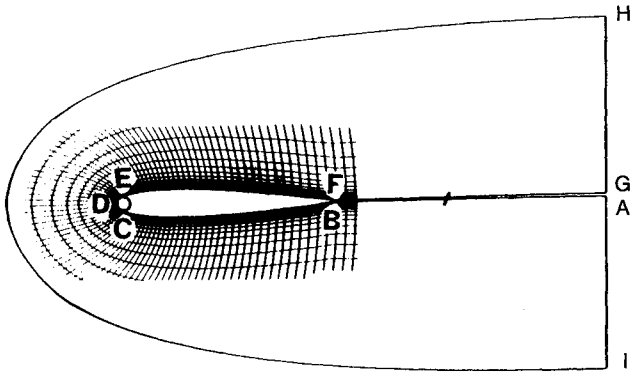

Fig. 1 Physical domain of interest in the present flowfield simulations.

and η as new independent variables, we recast Eq. (1) in the strongly conservative form given by

$$\partial_\tau \bar{q} + \partial_\xi \bar{E} + \partial_\eta \bar{F} = Re^{-1}(\partial_\xi \bar{R} + \partial_\eta \bar{S}) \tag{6}$$

Here,

$$\bar{q} = J^{-1}q \tag{7a}$$

$$\bar{E} = J^{-1}(\xi_x E + \xi_y F) \tag{7b}$$

$$\bar{F} = J^{-1}(\eta_x E + \eta_y F) \tag{7c}$$

$$\bar{R} = J^{-1}(\xi_x R + \xi_y S) \tag{7d}$$

$$\bar{S} = J^{-1}(\eta_x R + \eta_y S) \tag{7e}$$

In Eqs. (7), J is the Jacobian of the algebraic coordinate transformation, viz.,

$$J = \frac{\partial(x,y)}{\partial(\xi,\eta)} = x_\xi y_\eta - x_\eta y_\xi$$

U, V are the contravariant velocities given by

$$U = \xi_x u + \xi_y v$$

$$V = \eta_x u + \eta_y v$$

and ξ_x, η_x, ξ_y, η_y are the metrics of the coordinate transformation. For convenience, the grid increments $\Delta\xi$, $\Delta\eta$ are set equal to 1 in the rectangular computational plane.

Numerical Algorithm

Equation (6) is discretized in time using two-point backward first-order differencing and in space using three-point second-order central differencing, i.e.,

$$\delta_\tau \bar{q} + \Delta\tau(\delta_\xi \bar{E}^{n+1} + \delta_\eta \bar{F}^{n+1}) = \Delta\tau Re^{-1}(\delta_\xi \bar{R}^{n+1} + \delta_\eta \bar{S}^{n+1}) \tag{8}$$

Equation (8) is nonlinear, since the flux terms E and F are functions of the dependent variable q. Application of a Taylor series expansion to these terms results in the following linearized expressions for E and F at the new time level $(n+1)$, viz.,

$$\bar{E}^{n+1} = \bar{E}^n + A^n \Delta\bar{q}^n \tag{9a}$$

$$\bar{F}^{n+1} = \bar{F}^n + B^n \Delta\bar{q}^n \tag{9b}$$

Here, $A^n = (\partial_{\bar{q}} \bar{E})^n$, $B^n = (\partial_{\bar{q}} \bar{F})^n$, and $\Delta\bar{q}$ represent the change in the dependent variables $(\rho, \rho u, \rho v, e)$ at two successive time steps n, $n+1$. In Eqs. (9), A and B are commonly referred to as the Jacobian matrices of the flux vectors E, F. Rewriting Eq. (8), after utilizing the expressions given in Eqs. (9), and

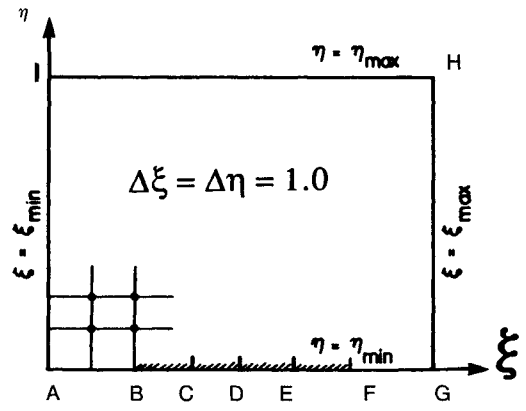

Fig. 2 Computational domain image of the physical domain depicted in Fig. 1.

rearranging, we obtain the following system of linear equations for Δq:

$$[I + \Delta\tau(\delta_\xi A^n + \delta_\eta B^n)]\Delta\bar{q}^n = -\Delta\tau(\delta_\xi \bar{E}^n + \delta_\eta \bar{F}^n) + \Delta\tau Re^{-1}(\delta_\xi \bar{R}^n + \delta_\eta \bar{S}^n) \tag{10}$$

As mentioned earlier, an approximate factorization scheme[18] was used in the present formulation to approximate the two-dimensional spatial differential operator appearing on the left-hand side of Eq. (10) as the product of two one-dimensional spatial operators in the ξ, η directions, respectively, i.e.,

$$[I + \Delta\tau\delta_\xi A^n][I + \Delta\tau\delta_\eta B^n]\Delta\bar{q}^n = -\Delta\tau(\delta_\xi \bar{E}^n + \delta_\eta \bar{F}^n) + \Delta\tau Re^{-1}(\delta_\xi \bar{R}^n + \delta_\eta \bar{S}^n) - (\Delta\tau)^2 \delta_\xi A^n \delta_\eta B^n \Delta\bar{q}^n \tag{11}$$

In Eq. (11), we further simplify the right side by neglecting the third term, which is of $\mathcal{O}(\Delta\tau)^2$, as compared to the first and second terms, which are $\mathcal{O}(\Delta\tau)$. As a result, Eq. (11) can be written as

$$[I + \Delta\tau\delta_\xi A^n][I + \Delta\tau\delta_\eta B^n]\Delta\bar{q}^n = \Delta\tau[RHS]^n \tag{12}$$

where

$$[RHS]^n = \Delta\tau[Re^{-1}(\delta_\xi \bar{R}^n + \delta_\eta \bar{S}^n) - (\delta_\xi \bar{E}^n + \delta_\eta \bar{F}^n)] \tag{13}$$

The solutions to Eq. (12) are then obtained using a two-step process through the introduction of an intermediate solution vector ΔT. Let

$$\Delta T = [I + \Delta\tau\delta_\eta B^n]\Delta\bar{q}^n \tag{14}$$

Then Eq. (12) can be expressed as

$$[I + \Delta\tau\delta_\xi A^n]\Delta T = \Delta\tau[RHS]^n \tag{15}$$

Application of Eqs. (14) and (15) at grid nodes inside the computational domain result in a matrix system with a block tridiagonal structure (having 4×4 coefficient matrices), which is solved efficiently using a lower-upper (LU) matrix decomposition procedure. Assuming that the dependent variables are known at time level n (or, equivalently, the corrections or delta quantities), the solution then proceeds by first solving Eq. (15) for ΔT, then Eq. (14) for $\Delta\bar{q}$. For steady-state solutions, Eqs. (14) and (15) are advanced in time at each grid node using a time step $\Delta\tau$ that is a function of the local transformation Jacobian,[19] i.e.,

$$\Delta\tau = \frac{1}{1 + \sqrt{J(i,j)}}$$

To prevent the odd-even point decoupling that results from the use of central difference operators on the left-hand side of Eq. (12), and to suppress the appearance of spurious solution oscillations in the vicinity of shock waves and stagnation points, second- and fourth-order dissipation terms are added to these equations. More precisely, implicit second-order dissipation terms in the ξ, η directions[19] are added to the left-hand side of Eq. (12), and a blend of "adaptive" second- and fourth-order explicit dissipation terms, in the manner suggested by Jameson et al.,[20] are added to the right-hand side of Eq. (12), viz.,

$$[I + \Delta\tau\delta_\xi A^n + \epsilon_I D_{I_\xi}][I + \Delta\tau\delta_\eta B^n + \epsilon_I D_{I_\eta}]\Delta\bar{q}^n$$

$$= \Delta\tau[(RHS)^n - \epsilon_E D_E] \tag{16}$$

In Eq. (16), the second-order dissipation operators are expressed as

$$D_{I_\xi} = -J^{-1}(\nabla_\xi \Delta_\xi J)$$

$$D_{I_\eta} = -J^{-1}(\nabla_\eta \Delta_\eta J)$$

and the explicit dissipation terms are expressed as

$$D_E = -\nabla_\xi[J^{-1}(\epsilon^2_{ij}\Delta_\xi q^n - \epsilon^4_{ij}\Delta_\xi \nabla_\xi \Delta_\xi q^n)] - \epsilon_E(\nabla_\eta \Delta_\eta)q^n$$

As seen, the added dissipation terms are usually of a higher order, i.e., on the order of $\Delta\xi^4$, $\Delta\eta^4$ and as such do not affect the formal second-order spatial accuracy of the numerical solutions. The coefficients ϵ^2_{ij}, ϵ^4_{ij} are adaptive coefficients that depend on the local pressure gradient determined using a "sensing" function σ_{ij}:

$$\sigma_{ij} = \frac{|P_{i+1} - 2P_i + P_{i-1}|}{|P_{i+1} + 2P_i + P_{i-1}|}$$

For example, near shock waves, the influence of the second-order explicit dissipation terms will be more dominant, as compared to the fourth-order dissipation terms. Near the leading edge, the opposite is true, with the fourth-order dissipation terms becoming more dominant. In Eq. (16), the constants ϵ_I, ϵ_E are used to control the amount of dissipation introduced in the solution. Note that ϵ_E is usually on the order of 1, and ϵ_I is typically 2–5 times larger. The numerical values of these coefficients are directly related to the freestream Mach number being considered. It should be mentioned here that the primary function of the implicit dissipation terms, when used in conjunction with explicit fourth-order dissipation, is to allow for the use of a larger time step and to increase the diagonal dominance of the coefficient matrices appearing on the left-hand side of Eq. (16). The reader is referred to Refs. 21–23 for additional results depicting the suitability and accuracy of the present dissipation model in the prediction of viscous transonic flows and unsteady separated flows.

Boundary Conditions

Referring to Figs. 1 and 2, we notice that the present time-dependent formulation requires boundary conditions to be specified along the coordinate lines ξ_{max}, ξ_{min}, η_{max}, η_{min}, and initial conditions (chosen to be those of the freestream) at grid nodes within the computational domain. In our solution approach, explicit boundary conditions are specified; that is, the delta quantities ΔT, $\Delta\bar{q}$ (or the flowfield corrections) are set to zero during the advancement of the solution by one time step. The flowfield variables, as well as some flow variables at the boundaries, are then computed as explained below.

Airfoil Surface (Boundary B-C-D-E-F)

On the stationary segments B-C, E-F of the airfoil, the no-slip boundary condition was enforced by setting the u and v components of the velocity vector V, or, equivalently, the contravariant velocities U, V to zero. For the moving segments C-D, D-E located in the vicinity of the leading edge, we introduce the nondimensional parameter β, defined as the ratio between the constant circumferential velocity of the cylindrical leading edge W divided by the freestream speed of sound. In this respect, β may also be considered as a Mach number associated with the leading-edge moving segments. In the present formulation, slip boundary conditions were prescribed on the segments C-D, D-E of the computational domain boundary $\eta = \eta_{min}$, i.e.,

$$W \cdot e = 0$$

Here, e is the outward local unit vector in the direction normal to the moving leading-edge segments. The velocity components associated with the grid points lying along C-D, D-E are thus given by

$$u = W\cos(\theta), \qquad v = W\sin(\theta)$$

with θ being the local slope at grid nodes on the moving cylindrical leading edge. For all "stationary" surface grid points, the density ρ and pressure p were computed using the following three-point difference expressions:

$$\rho(i, 1) = 2\rho(i, 2) - \rho(i, 3)$$

$$p(i, 1) = [4p(i, 2) - p(i, 3)]/3$$

The first expression implies that the density at the surface is extrapolated using the density values at the two grid nodes just off the surface. The second-difference expression for the surface pressure is an approximation for a vanishing pressure gradient on the stationary solid wall. At all grid locations lying on the rotating portion of the leading edge, the two momentum equations were evaluated at the surface of the airfoil using limiting expressions. In this respect, normal pressure variations due to centrifugal effects were accounted for. In our calculations, an adiabatic wall condition was assumed at all grid nodes on the airfoil's surface. The surface total energy was determined using Eqs. (4) and (5), once the surface pressure and density were computed.

Wake Branch Cut (Segments A-B, F-G)

Continuity of the physical flow properties across the branch cut A-B, F-G requires that

$$q(\xi_A \le \xi \le \xi_B, \eta_{min}) = q(\xi_F \le \xi \le \xi_G, \eta_{min})$$

In the present formulation, this condition was satisfied by averaging linear extrapolates of the computed flowfield variables from above and below the branch cut.

Far-Field Boundary (G-H-I-A)

We take advantage of the characteristic features of a subsonic inflow and/or outflow boundary.[24] At the computational domain boundary representing the inflow boundary of the far field, i.e., $\eta = \eta_{max}$ in Fig. 2, the characteristics of the inviscid Euler equations [i.e., Eq. (1) after neglecting the right-hand side] a priori determine the number and type of variable(s) (e.g., ρ, u, v, etc.) that can be specified at this boundary. The remaining variables are then determined explicitly through extrapolations from the inner domain solutions, and are thus determined as part of the numerical solution. At the downstream boundary (i.e., $\xi = \xi_{min}$, $\xi = \xi_{max}$), the density ρ and velocity components u, v are extrapolated from the interior. The pressure p is held fixed at the freestream pressure, and the total energy/unit volume e is computed using Eq. (4).

Experimental Facility

The smoke wire flow visualization experiments were performed in an open circuit indraft-type wind tunnel having a rectangular test section (0.0875 m width × 0.25 m height). The tunnel is capable of producing air speeds in the range of 0.25–6.5 m/s, but was typically operated at 1–2 ms. At the maximum speed, the fluctuations in the mean flow were on the order of 1.5%, and turbulence levels ($\hat{u}/U_\infty$) were on the order of 1.5–2% close to the walls. A bell mouth with an area contraction ratio of 56:1 was placed at the entrance to the test section. This was followed by two sections containing an antiturbulence honeycomb screen (length/diameter ratio = 10.7, 95.7% porosity) and drinking straws to straighten and smooth out the flow prior to reaching the test section. The combination of antiturbulence screen, flow straightener, and large inlet contraction provides a uniform velocity profile with a turbulence intensity of 0.5% in the tunnel test section at an air speed of 1.65 m/s. The test section is designed with a large plexiglass window in the top for easy access to the model and plexiglass sides to provide for adequate illumination and viewing for visualization studies. Following the test section, the flow was expanded in a diffuser. The tunnel was powered by a 5.6 kW motor operating a centrifugal blower at the downstream end of the diffuser section.

Spanning the test section is the wing model (NACA 0015 section), having a 0.175 m chord with a 0.0275 m maximum thickness. The model was sprayed with flat-black paint to minimize light reflections from its smooth surface. At 5-deg angle of attack, the blockage ratio in the test section is 0.1125. A rotating cylinder (radius = 5 mm) representing the leading edge of the test model was selected to match the average curvature of the leading edge of the basic NACA 0015 section. To allow the cylinder to rotate freely, a gap of 0.5 mm in width was left between the rotating cylinder and the remaining stationary part of the wing. Different angular speeds were directly imparted to the model's leading edge using a variable speed motor (5,000–28,000 rpm) and high-speed still photography (10 frames/s) was utilized to capture the details of the flowfield. A 0.09-mm-diam Nichrome smoke wire was placed 30 mm ahead of the model's leading edge, perpendicular to the axis of rotation at midspan point. In the experiments, a time delay circuit similar to that utilized by Batill and Mueller[25] was utilized to trigger the high-speed camera approximately one tenth of a second before the smoke wire circuit was activated.

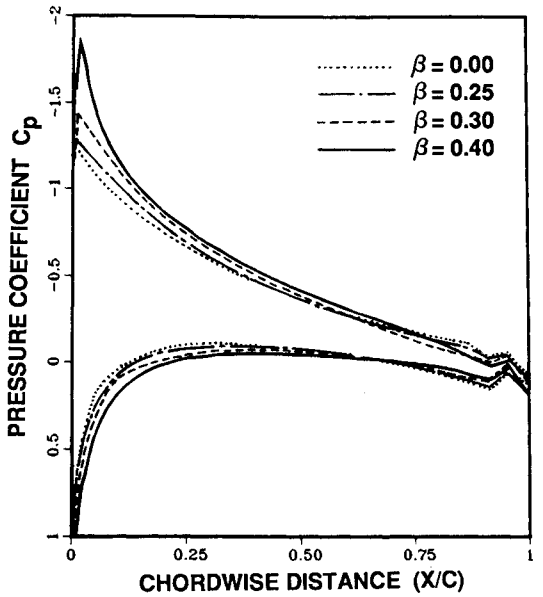

Fig. 3 Predicted surface pressure distributions for the flow past the modified NACA 0012 airfoil (*Eminf* = 0.283, *Re* = 3.45 × 10⁶, α = 5 deg, transition at *x/c* = 0.0).

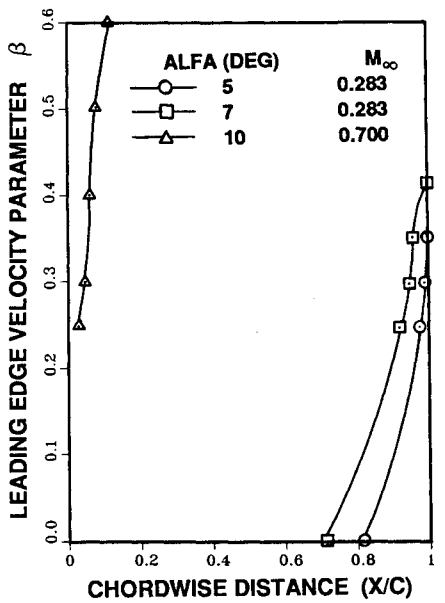

Fig. 4 Predicted locations of the upper surface turbulent separation points as a function of the leading-edge rotational speed for the modified NACA 0012 airfoil (*Re* = 3.45 × 10⁶).

Results and Discussion

The parameter of prime importance in the present study is the nondimensional leading-edge parameter β. It should be emphasized here that an increase in the magnitude of β would imply a direct increase in the strength of the FBIV (or, alternatively, an increase in the introduced leading-edge momentum) and vice versa.

Figure 3 depicts the effect of varying β on the computed surface pressure distributions for the modified NACA 0012 airfoil at a freestream Mach number of 0.283, an angle of attack α of 5 deg, and a chord Reynolds number of 3.45 × 10⁶. For contrast, the results for the original airfoil (i.e., β = 0) are also shown. In these simulations, transition to turbulent flow was assumed to occur at the airfoil's leading edge. As seen, the leading-edge wall-jet-like effect results in an increase (in a negative sense) in the predicted leading-edge suction pressure

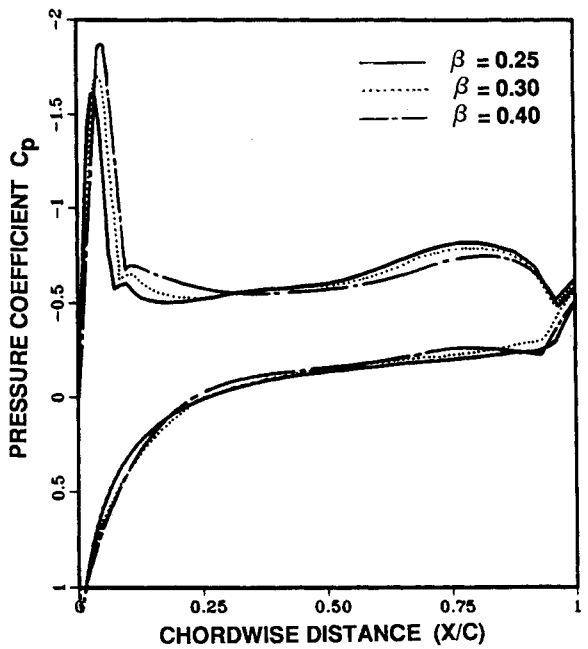

Fig. 5 Predicted surface pressure distributions for the flow past the modified NACA 0012 airfoil (*Eminf* = 0.70, *Re* = 3.45 × 10⁶, α = 10 deg, transition at *x/c* = 0).

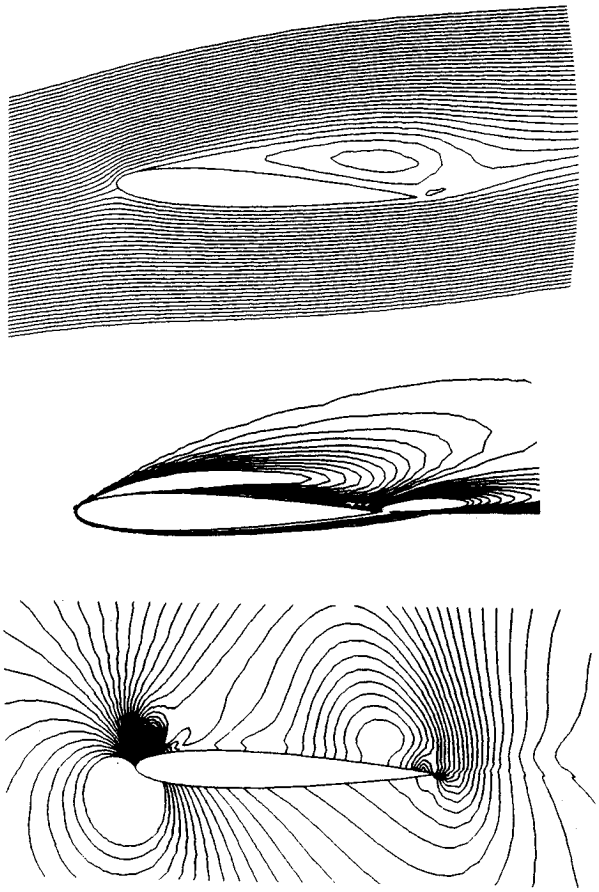

Fig. 6 Streamline patterns, constant vorticity contours, and isobars for the flow past the modified NACA 0012 airfoil having leading-edge rotation (*Eminf* = 0.70, *Re* = 3.45 × 10⁶, α = 10 deg, β = 0.5, transition at x/c = 0).

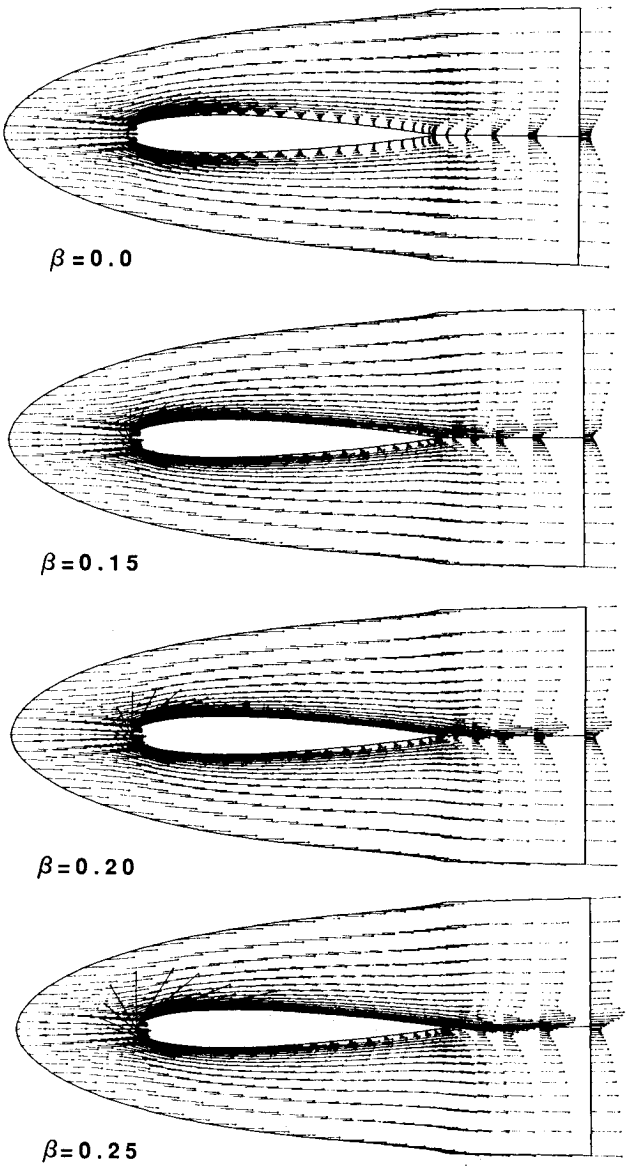

Fig. 7 Predicted near-field velocity vector plots as a function of the leading-edge rotational speed for the flow past the modified NACA 0012 airfoil (*Eminf* = 0.5, *Re* = 8 × 10⁴, α = 0 deg, laminar flow).

peaks. Moreover, the increase in the magnitude of this peak seems to increase in direct proportion to the increase in the leading-edge parameter β. The variation in the locations of the predicted upper surface turbulent separation points as a function of β is illustrated in Fig. 4. Note that for a freestream Mach number of 0.283 and an angle of attack of 5 deg, complete reattachment of the turbulent boundary layer takes place for values of β larger than 0.335. For the same freestream Mach number and an angle of attack of 7 deg, complete reattachment occurs for values of β larger than 0.42. Numerical results have further indicated that, for values of β larger than 0.335 and 0.42, only an increase in the predicted sectional lift was observed. This is, of course, a direct consequence of the increase in the leading-edge suction pressure peaks.

The predicted surface pressure distributions as a function of β for a freestream Mach number of 0.70, a chord Reynolds number of 3.45×10^6, and an angle of attack of 10 deg for the modified NACA 0012 airfoil section are illustrated in Fig. 5. In this particular example, the wall-jet-like effect results in an increase in the local Mach number of the accelerating flow in the vicinity of the leading edge. As a result, a leading-edge shock is formed. Numerical results have indicated a direct increase in the strength of the leading-edge shock and the size of the small supercritical flow region in the vicinity of the rotating leading edge with further increase in the parameter β. Observe in Fig. 5 that the leading-edge shocks are slightly displaced downstream towards the trailing edge with the increase in β. The shock-induced separation points (coinciding with the locations of the leading-edge shocks) are also being displaced towards the trailing edge (see Fig. 4). It is noteworthy to mention that, in our attempts to propagate the leading-edge shocks towards the trailing edge, no values of the parameter β were found to be sufficient to change the overall structure of the flowfield beyond the point of turbulent separation. Moreover, a rapid increase in the predicted drag was noticed with the slight increase in the predicted lift. In Fig. 6, we illustrate the predicted streamline patterns, constant vorticity contours, and isobars, respectively, for the flow past the modified NACA 0012 airfoil with leading-edge rotation (β = 0.5).

The predicted near fields as a function of the leading-edge parameter β for the laminar flow past the modified NACA 0012 airfoil at a freestream Mach number of 0.5, chord Reynolds number of 8×10^4, and angles of attack 0, 10, 15, and 25 deg are illustrated in Figs. 7–10, respectively. With the increase in the magnitude of β, the velocity vector plots depict considerably different flowfield features for the various angles of attack considered. For low to moderate angles of attack (i.e., varying in the range 0–10 deg), we notice the following with the increase in the parameter β: 1) the migration of the upper surface separation point towards the trailing edge until a value of β is reached where full reattachment occurs, and 2) a reduction in the height of the upper surface laminar separation flow region followed by a "squeezing" effect, for higher values of β, of the upper surface concentrated vortical flow

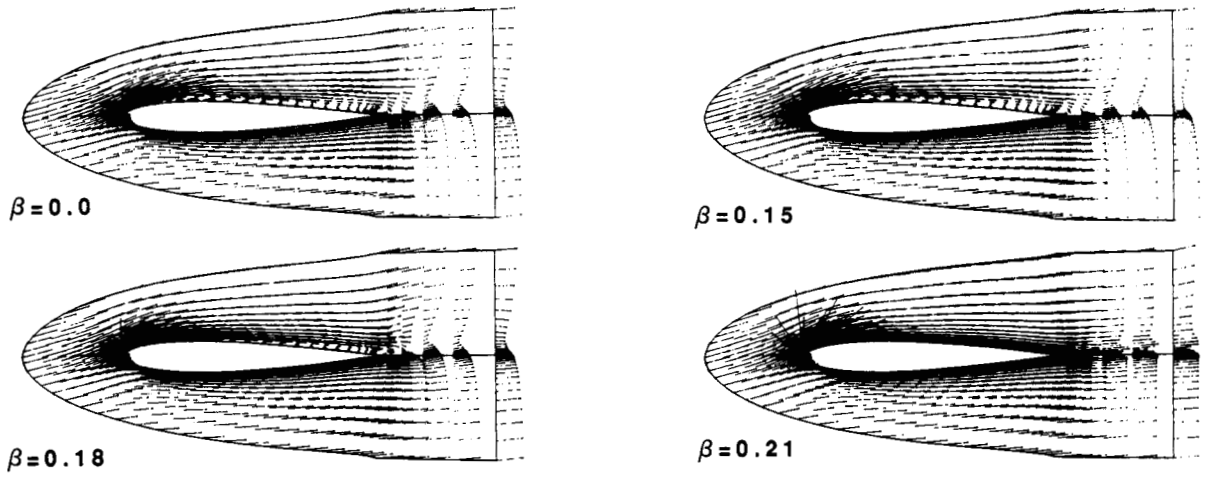

Fig. 8 Predicted near-field velocity vector plots for the flow past the modified NACA 0012 airfoil (*Eminf* = 0.50, $Re = 8 \times 10^4$, $\alpha = 10$ deg, laminar).

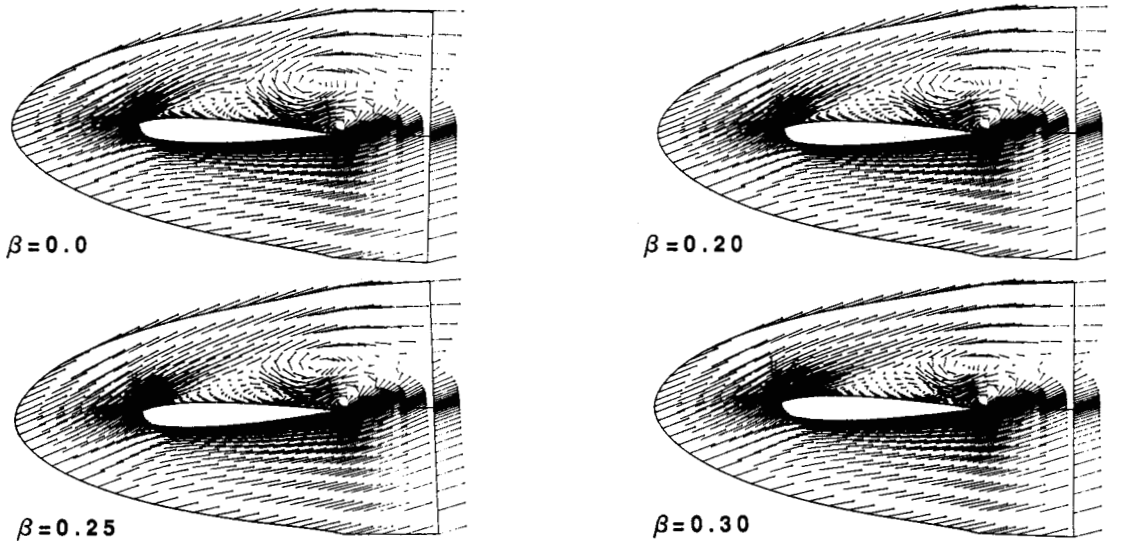

Fig. 9 Predicted near-field velocity vector plots for the flow past the modified NACA 0012 airfoil (*Eminf* = 0.50, $Re = 8 \times 10^4$, $\alpha = 15$ deg, laminar).

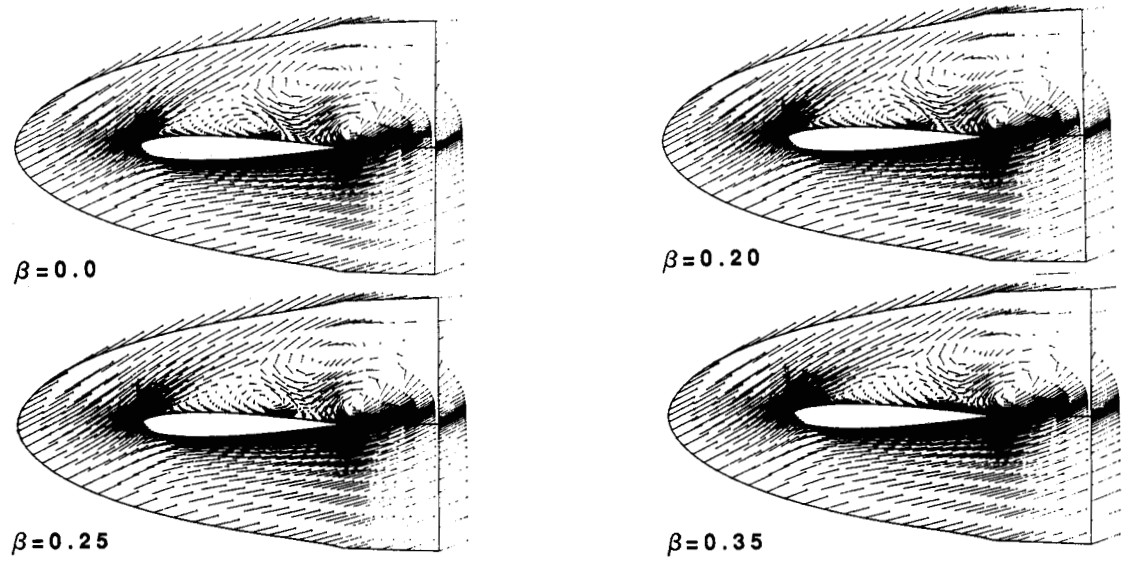

Fig. 10 Predicted near-field velocity vector plots for the flow past the modified NACA 0012 airfoil (*Eminf* = 0.50, $Re = 8 \times 10^4$, $\alpha = 20$ deg, laminar).

towards the trailing edge and eventually into the wake region. On the other hand, for the high angles of attack considered (i.e., those higher than 10 deg), we notice that only a thin layer of fluid, whose extent along the surface depends largely on the magnitude of the parameter β, remains attached to the surface of the airfoil. It should be noted that complete reattachment of the boundary layer in the "familiar" sense was not achieved for all the values of β considered in this study. However, a slight reduction in the height of the separated free shear layer was obtained with the increase in the magnitude of β. These observations also agree with those made by Ref. 26 using an explicit solution procedure of the laminar Navier-Stokes equations.

The smoke wire flow visualization results for the flow past a modified NACA 0015 airfoil (chord Reynolds number of 9.7×10^4 and angle of attack of 5 deg) having leading-edge rotation are depicted in Figs. 11 and 12. In this section, we redefine the leading-edge parameter β as the ratio of the circumferential velocity of the rotating leading edge to the freestream velocity (instead of the freestream speed of sound, as we have done previously in our compressible flow numerical simulations). Figure 11 illustrates the variation of the size of the upper surface separation flow region as a function of the leading-edge parameter β. The trailing-edge position can be easily identified in the photographs by the light reflected off its upper surface. In Fig. 11c, notice that the laminar boundary layer has undergone transition at a position that approximately coincides with that of the gap between the rotating leading edge and the remainder of the airfoil. This observation prompted the choice of the leading-edge position to be that where laminar-turbulent transition was enforced when conducting the turbulent flow numerical simulations. Figure 11c illustrates the complete reattachment of the turbulent boundary layer for a value of β equal to 6.06. The resulting flowfield henceforth became independent of β, and its main features remained unaltered with any further increase in the leading-edge parameter. In Fig. 12, we illustrate the streamline patterns in the immediate vicinity of the rotating leading edge as a function of β. Clearly, Fig. 12c depicts a more pronounced leading-edge suction region, as compared to those in Figs. 12a and 12b, merely by considering the number of streamlines drawn towards the upper surface as a function of β. This observation is quite in agreement with our predictions of the leading-edge suction pressure peaks. It is important to mention here that what seem to be streamlines emanating from the surface of the airfoil in Fig. 12c are actually streamlines that have been drawn too close to the rotating leading edge and have not been clearly resolved in the photograph due to inadequate lighting.

A comparison between the predicted and measured[13] sectional lift coefficients for the turbulent flow past a modified

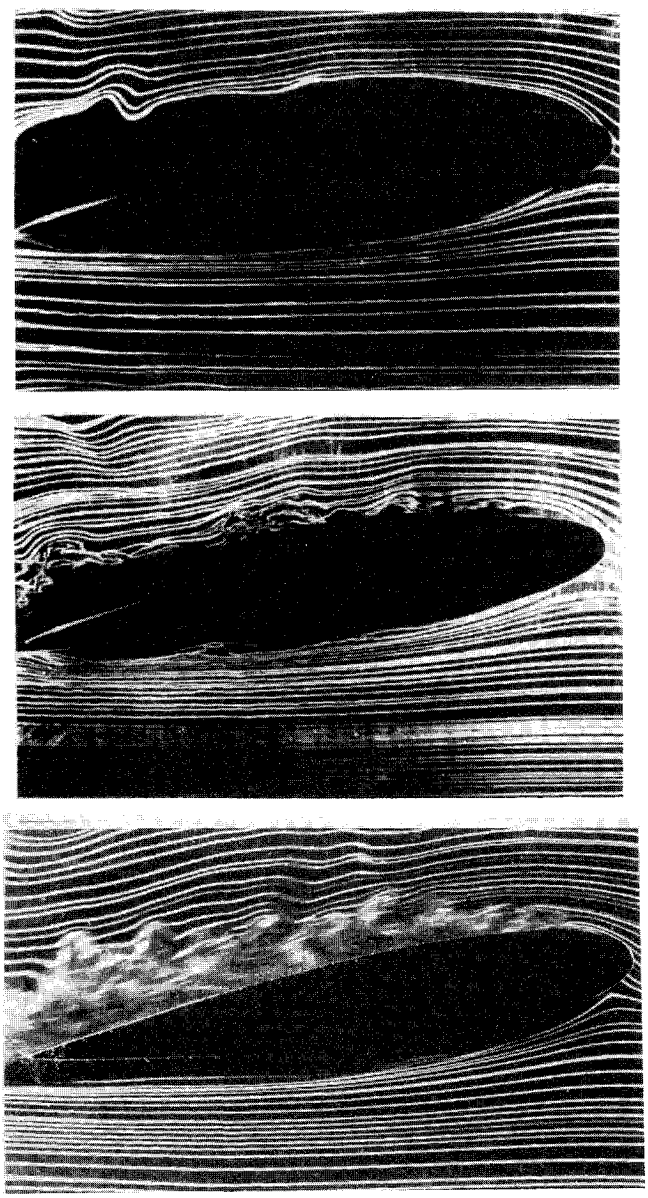

Fig. 11 Smoke wire flow patterns representing the changes in the structure of the originally laminar boundary layer as a function of the leading-edge circumferential speed for the flow past a modified NACA 0015 airfoil ($Re = 9.7 \times 10^4$, $\alpha = 5$ deg).

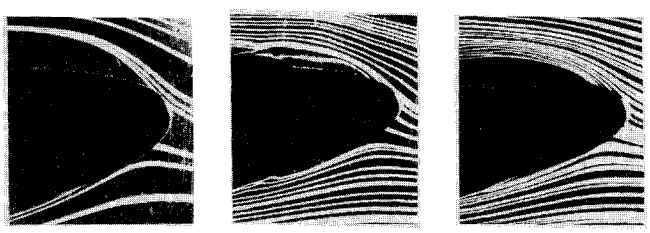

Fig. 12 Smoke wire flow patterns in the vicinity of the leading edge of the modified NACA 0015 airfoil ($Re = 9.7 \times 10^4$, $\alpha = 5$ deg).

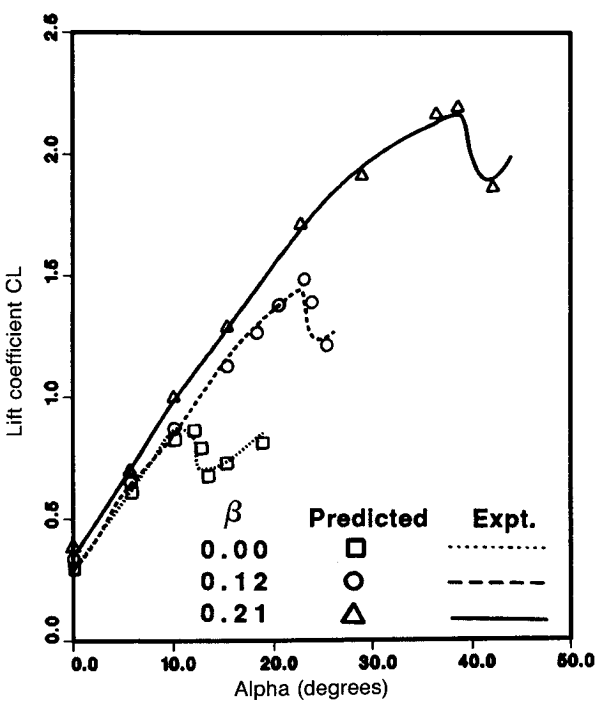

Fig. 13 A comparison between the predicted and measured sectional lift characteristics for a modified NACA 63-218 airfoil ($Eminf = 0.10$, $Re = 2.9 \times 10^6$, transition at $x/c = 0.0$).

NACA 63-218 airfoil having leading-edge rotation is given in Fig. 13.

At this juncture, it is important to mention that, in conducting our numerical simulations, experimentation with the number of grid points at which slip boundary conditions were specified was necessary to obtain an acceptable correlation with the experimental data. For example, whereas the use of a few number of grid nodes resulted in the underprediction of the lift forces, a large number of grid nodes, on the other hand, usually resulted in an overprediction of the lift forces. This experimentation was primarily due to the incomplete geometric construction details for the tested model, specifically for the leading-edge region. As seen, very good correlation with the data is obtained for the three values of β considered. The choice of the full Reynolds-averaged Navier-Stokes formulation to conduct the present simulations was also necessary to predict the flowfield features at angles of attack approaching and exceeding the static stall angle of the airfoil.

Conclusions

An analysis has been presented for computing the flowfield past airfoils having leading-edge rotation in both subcritical and supercritical onset flows. For the subcritical flows considered, the wall-jet-like effects produced by the rotating leading edge resulted in a reduction in the size or the complete elimination of the upper surface separated flow region. As a result, an increase in the sectional lift forces could be achieved with such a leading-edge device. However, the gained benefits resulting from the introduction of vorticity in the leading-edge region tend to decrease with the continuous increase in the flow angle of attack. For supercritical flows, the early formation of a leading-edge shock wave inhibits the beneficiary effects of the additional momentum introduced into the boundary layer through the rotating leading edge. Despite the slight increase in the predicted sectional lift forces, the accompanying rapid increase in the drag forces does not warrant the use of this device as means to control the boundary layer at supercritical or perhaps critical onset flow conditions. The computed subcritical onset flow results compared well with the qualitative (overall flowfield features) and quantitative (lift data) experimental data available. Extensions to the present work will include a study of the effects of FBIV on the development of the flow past an airfoil undergoing unsteady pitch oscillations.

Acknowledgment

The first author would like to thank E. Logan of Arizona State University for allowing the use of his wind-tunnel facility and M. M. Rahman for providing the velocity vector plotting routines for the laminar flow results. The free computer time provided by Arizona State University for conducting the laminar flow simulations while the first author was a faculty member is also acknowledged.

References

[1]Kuchemann, D., *The Aerodynamic Design of Aircraft,* Pergamon, Oxford, England, UK, 1978.

[2]Orlick-Ruckemann, K. J., "Aerodynamic Aspects of Aircraft Dynamics at High Angles of Attack," *Journal of Aircraft,* Vol. 20, No. 9, 1983, pp. 737–752.

[3]Ericsson, L. E., and Reding, J. P., "Dynamics of Forebody Flow Separation and Associated Vortices," *Journal of Aircraft,* Vol. 23, No. 4, 1985, pp. 329–335.

[4]Gregory, N., and Walker, W. S., "Wind Tunnel Tests on the NACA 63A009 Aerofoil with Distributed Suction Over the Nose," ARC RM-2900, 1955.

[5]Wood, N. J., and Roberts, L., "Control of Vortical Lift on Delta Wings by Tangential Leading-Edge Blowing," *Journal of Aircraft,* Vol. 25, No. 3, 1988, pp. 236–243.

[6]Lachmann, G. V., *Boundary Layer and Flow Control,* Vols. I and II, Pergamon, Oxford, England, UK, 1961.

[7]Rosenhead, L., *Laminar Boundary Layers,* Oxford Univ., Oxford, England, UK, 1966.

[8]Schlichting, H., *Boundary Layer Theory,* McGraw-Hill, New York, 1968.

[9]Chang, P. K., *Separation of Flow,* Pergamon, Oxford, England, UK, 1970.

[10]Kothari, A. P., and Anderson, J. D., "Computational Study of Flow Over Miley and Wortmann Airfoils," *Proceedings of the Conference on Low Reynolds Number Airfoil Aerodynamics,* Univ. of Notre Dame, Notre Dame, IN, June 1985, pp. 235–254.

[11]Wolff, F. B., and Koning, C., "Tests for Determining the Effect of a Rotating Cylinder Fitted into the Leading Edge of an Airplane Wing," NACA TM-354, 1926.

[12]Sayers, A. T., "Lift Coefficient and Flow Visualization on a Leading Edge Rotating Cylinder Rudder," *International Journal of Mechanical Engineering Education,* Vol. 7, No. 2, 1979, pp. 114–121.

[13]Modi, V. J., Sun, J. L. C., Akutsu, T., Lake, P., and McMillan, K., "Moving Surface Boundary Layer Control For Aircraft Operation at High Incidence," AIAA Paper 80-1621, 1980.

[14]Moktarian, F., and Modi, V. J., "Fluid Dynamics of Airfoils with Moving Surface Boundary-Layer Control," *Journal of Aircraft,* Vol. 25, No. 2, 1988, pp. 163–169.

[15]Baldwin, B. S., and Lomax, H., "Thin Layer Approximation and Algebraic Model for Separated Turbulent Flows," AIAA Paper 78-257, Jan. 1978.

[16]Wu, J. C., "A Study of Unsteady Turbulent Flow Past Airfoils," Ph.D. Thesis, School of Aerospace Engineering, Georgia Inst. of Technology, Atlanta, GA, Aug. 1988.

[17]Jameson, A., "Iterative Solutions of Transonic Flow Over Airfoils and Wings Including Flows at Mach 1," *Communication on Pure Applied Mathematics,* Vol. 27, 1974, pp. 283–309.

[18]Beam, R. M., and Warming, R. F., "An Implicit Factored Scheme for the Compressible Navier-Stokes Equations," *AIAA Journal,* Vol. 16, No. 4, 1976.

[19]Pulliam, T. H., and Steger, J. L., "Recent Improvements in Efficiency, Accuracy, and Convergence for Implicit Approximate Factorization Algorithms," AIAA Paper 85-0360, Jan. 1985.

[20]Jameson, A., Schmidt, W., and Turkel, E., "Numerical Solutions of the Euler Equations by Finite-Volume Methods Using Runge-Kutta Time-Stepping Schemes," AIAA Paper 81-1259, June 1981.

[21]Tassa, Y., and Sankar, L. N., "Dynamic Stall of NACA 0012 Airfoil in Turbulent Flow—Numerical Study," AIAA Paper 81-1289, June 1981.

[22]Sankar, L. N., and Tang, W., "Numerical Solution of Unsteady Viscous Flow Past Rotor Sections," AIAA Paper 85-0129, Jan. 1985.

[23]Tang, W., "Numerical Solutions of Unsteady Flow Past Rotor Sections," Ph.D. Dissertation, Georgia Inst. of Technology, Atlanta, GA, Sept. 1986.

[24]Hedstrom, G. W., "Nonreflecting Boundary Conditions for Nonlinear Hyperbolic Systems," *Journal of Computational Physics,* Vol. 30, No. 3, 1979, pp. 222–237.

[25]Batill, S. M., and Mueller, T. J., "Visualization of Transition in the Flow Over an Airfoil Using the Smoke Wire Technique," *AIAA Journal,* Vol. 19, No. 3, 1981, pp. 340–345.

[26]Hassan, A. A., and Rahman, M. M., "On the Wall Jet-Like Effects of a Moving Boundary," *Proceedings of the International Conference on Computational Engineering Science,* Vol. 2, Springer-Verlag, New York, April 1988.